metals

Article

Corrosion Behavior of AISI 52100 Bearing Steel in Novel Water-Based Lubricants

Juan Bosch *, Elizabeth Kotzalas, K Zin Htut, Rowan King and Christopher DellaCorte

Akron Engineering Tribology Laboratory, The University of Akron, Akron, OH 44325, USA; elk38@uakron.edu (E.K.); kh118@uakron.edu (K.Z.H.); ark176@uakron.edu (R.K.); cdellacorte@uakron.edu (C.D.)
* Correspondence: jb394@uakron.edu

Abstract

Water-based lubricants (WBLs) are increasingly being considered for electrified drivetrain applications; however, their electrochemical stability toward bearing steels remains insufficiently understood. This study evaluated the corrosion behavior of through-hardened AISI 52100 bearing steel in novel WBLs to elucidate the corrosion kinetics and surface degradation mechanisms. Round steel disks were cleaned and tested in 50 wt% aqueous dilutions of glycerol, ethylene glycol (MEG), polyethylene glycol (PEG), and polyalkylene glycol (PAG). Electrochemical measurements were conducted using a three-electrode cell in accordance with ASTM G3-14, employing open circuit potential (OCP), linear polarization resistance (LPR), electrochemical impedance spectroscopy (EIS), and potentiodynamic polarization curves. Among the uninhibited fluids, DI water exhibited the highest corrosion current density (19.85 $\mu A/cm^2$), while glycerol- and PEG-based systems showed the lowest values (0.79 and 0.85 $\mu A/cm^2$, respectively), attributed to organic adsorption at the steel/electrolyte interface. EIS analysis revealed a single charge-transfer-controlled process across all fluids, consistent with a weak, non-passive interfacial oxide whose protective character is modulated by organic adsorption. The addition of $NaNO_3$ produced divergent effects depending on the base fluid chemistry: the corrosion activity was reduced in DI water and glycerol systems through enhanced passivation, while PEG- and PAG-based formulations showed increased corrosion current densities and reduced charge transfer resistance, attributed to competitive disruption of the polymer boundary layer by nitrate ions. Surface characterization by SEM/EDAX and white-light interferometry corroborated the electrochemical findings, revealing fluid-dependent corrosion morphologies ranging from uniform attack in DI water to localized pitting in polymer-based systems, with $NaNO_3$ shifting the corrosion mode in PEG/PAG systems from localized to combined localized and uniform attack. These findings highlight the critical role of fluid chemistry in controlling corrosion processes in water-based lubricants and provide mechanistic insight for the development of corrosion-stable formulations for high-performance electrified drivetrain applications.

Keywords: water-based lubricants; bearing steel degradation; electro-tribocorrosion

Check for updates

Academic Editor: Eric Hug

Received: 4 March 2026
Revised: 4 April 2026
Accepted: 8 April 2026
Published: 15 April 2026

Copyright: © 2026 by the authors. Licensee MDPI, Basel, Switzerland. This article is an open access article distributed under the terms and conditions of the Creative Commons Attribution (CC BY) license.

1. Introduction

The rapid expansion of electric vehicles (EVs), including battery electric (BEV), hybrid electric (HEV), plug-in hybrid (PHEV), and fuel cell (FCEV) platforms, is fundamentally reshaping lubricant design requirements. Unlike internal combustion engine (ICE) vehicles, where lubricant formulations have been largely driven by combustion-related constraints,

electrified powertrains integrate electric motors, gears, bearings, and power electronics into compact architectures operating at higher rotational speeds and power densities [1–4]. These changes have intensified interest in multifunctional fluids capable of simultaneously providing lubrication and thermal management. In this context, water-based lubricants (WBLs), defined as fluids containing ≥50 wt.% water, and water-containing lubricants (WCLs, <50 wt.% water) have attracted increasing attention due to their high thermal conductivity, low viscosity, and reported friction reduction capabilities [2,5–9]. Recent industry reports further indicate growing original equipment manufacturer (OEM) interest in such fluids to improve energy efficiency and reduce system complexity [2].

Substantial tribological research has demonstrated that water-containing polyalkylene glycols (PAGs), glycerol mixtures, and related aqueous systems can achieve low friction and even superlubricity under certain elastohydrodynamic (EHL) and boundary lubrication conditions [7–12]. For example, water-containing PAGs have been shown to produce friction coefficients below 0.01 in rolling-sliding contacts [9,13,14], and glycerol–water mixtures have exhibited significant friction reductions compared to conventional polyalphaolefin (PAO) oils [8,15–17]. These effects have been attributed to reduced pressure–viscosity coefficients, formation of low-shear hydrated layers, and tribofilm development under sliding conditions [8,10,18–22]. However, increasing water concentration reduces film thickness and can promote transitions from full film to mixed or boundary lubrication at high speeds or loads [8,16], highlighting the complex interplay between rheology and lubrication regime.

Despite these advances in friction and film formation, the electrochemical compatibility of WBLs with bearing steels remains comparatively underexplored. High water content fundamentally alters interfacial chemistry and can promote anodic dissolution, modify passivation behavior, and increase susceptibility to localized corrosion, particularly in high-strength steels such as AISI 52100 commonly used in rolling element bearings [23]. Conditions relevant to EV drivetrains, including elevated temperatures, dissolved oxygen, and stray electrical potentials, may further accelerate corrosion processes. To mitigate these effects, corrosion inhibitors such as sodium nitrate ($NaNO_3$) may be incorporated to promote passivation of AISI 52100 steel through stabilization of protective iron oxide films, thereby suppressing anodic dissolution and reducing corrosion current density in high-water-content lubricant environments.

This issue is critical for enabling a single-fluid approach, wherein a single aqueous lubricant serves both cooling and lubrication functions within electrified powertrains. While WBLs offer enhanced heat dissipation and reduced viscous losses, their adoption as primary drivetrain fluids requires assurance that corrosion rates, passivation stability, and surface degradation remain within acceptable limits. Recent tribocorrosion studies on GCr15 steel (equivalent to AISI 52100) have shown that water–glycol fluids can alter reaction film composition and wear behavior under aggressive environments [24]. Similarly, investigations of aqueous lubricant systems containing ionic additives have demonstrated that water-rich media influence oxide tribofilm formation on AISI 52100, affecting both friction and corrosion pathways [23]. These findings underscore the coupled nature of tribological and electrochemical degradation in aqueous lubricant environments.

Similar aqueous-glycol environments are widely encountered in automotive engine cooling systems, where water–ethylene glycol mixtures are used for thermal management. In these systems, steel and cast iron components are exposed to water–glycol solutions containing corrosion inhibitors designed to control anodic dissolution and stabilize protective oxide films. Previous studies showed that corrosion behavior in such coolant environments strongly depends on glycol concentration, oxygen availability, and inhibitor chemistry [25,26]. While the corrosion of metals in automotive coolants has been studied

extensively, these systems are primarily designed for heat transfer rather than lubrication. As a result, the electrochemical behavior of bearing steels in high-water-content lubricants remains less understood, particularly when such fluids are proposed as multifunctional lubricants and coolants in electrified drivetrains.

In addition to conventional water–glycol coolant systems, increasing attention has been directed towards polyol-based aqueous solutions, including glycerol and polyethylene glycol containing solutions, due to their potential to modify corrosion behavior through interactions at the metal–electrolyte interface. Glycerol based systems have been reported to exhibit reduced corrosion activity relative to purely aqueous environments, attributed to their increased solution viscosity, reduced oxygen transport, and the formation of adsorbed surface films that enhance passivation stability [27–29]. Similarly, polyethylene glycol (PEG) has demonstrated the ability to influence electrochemical behavior through adsorption-driven mechanisms, contributing to the formation of protective interfacial layers and reduced corrosion current densities in aqueous systems [30]. In contrast, lower molecular weight aqueous glycol systems such as ethylene glycol may exhibit more complex behavior due to chemical degradation processes; oxidation of ethylene glycol can generate organic acids, which reduce solution pH and accelerate anodic dissolution of steel surfaces [31]. Furthermore, corrosion behavior in aqueous glycol solutions has been shown to depend strongly on water content and solution chemistry, with higher water fractions promoting increased electrochemical activity [32]. While recent studies on glycol-based heat transfer fluids demonstrated the importance of inhibitor chemistry in mitigating corrosion processes [33], these systems have been typically optimized for thermal management rather than lubrication. Consequently, a systematic understanding of corrosion mechanisms across glycerol, PEG, and glycol-based water-based lubricants remains limited, particularly for bearing steels operating in high-water content environments.

While these studies provide important mechanistic insight, systematic electrochemical evaluation of neat WBL base fluids ($\geq$50 wt.% water) remains limited. Much of the literature emphasizes additive-enhanced formulations or WCL systems (<50 wt.% water), leaving intrinsic corrosion kinetics, passivation characteristics, and polarization responses of high-water-content WBLs insufficiently characterized. This knowledge gap limits engineering assessment of WBLs as primary lubricating fluids because water-induced corrosion may offset gains in friction reduction and thermal performance.

Accordingly, this work investigated the corrosion behavior and inhibition of WBLs in contact with AISI 52100 bearing steel using open circuit potential (OCP) monitoring and potentiodynamic polarization techniques. The objective was to quantify electrochemical stability, compare corrosion kinetics across lubricant chemistries, and assess the feasibility of WBLs for single-fluid EV drivetrain lubrication.

2. Materials and Methods

Round disks made of through-hardened AISI 52100 bearing steel(McMaster-Carr, Aurora, OH, USA) were used to study their electrochemical response under different solutions. The elemental composition of AISI 52100 can be seen in Table 1. The disks had a diameter of 15.875 mm and a thickness of 10 mm; prior to the electrochemical tests the samples were degreased in an ultrasonic cleaner with hexane and isopropyl alcohol (VWR, Radnor, PA, USA) and air dried.

Table 1. AISI 52100 steel elemental composition in wt.%.

C	Mn	Si	Cu	S	P	Ni	Cr	Si	Mo	Al	Ti	Fe
0.95	0.35	0.25	0.16	0.001	0.01	0.12	1.54	0.20	0.028	0.009	0.003	Bal.

The WBLs studied were prepared using 50 wt.% dilutions of deionized water and either glycerol (VWR, Radnor, PA, USA), ethylene glycol (MEG) (VWR, Radnor, PA, USA), polyethylene glycol (PEG) (Sigma Aldrich, 99%, St. Louis, MO, USA), and polyalkylene glycol (PAG) (BASF, Florham Park, NJ, USA). The 500 mL dilutions were mixed at 50 °C with a magnetic stirrer at 500 rpm for 45 min in a sealed container to prevent water evaporation. The properties of the fluids can be seen in Table 2, obtained from ref. [34]. Among the most important properties for lubricants is the pressure–viscosity coefficient (α_0). This coefficient indicates how thick lubricant films will become in elastohydrodynamic lubricated contacts [35]. Sodium nitrate ($NaNO_3$) (Sigma Aldrich, St. Louis, MO, USA) was incorporated as a corrosion inhibitor at a 0.2 wt.% of solution; this treatment level is common in lubricant applications [36].

Table 2. Fluid properties of the different water-based lubricants, adapted from [34].

Fluid	pH	Density (g/mL)	α_0 (GPa^{-1})	Kinematic Viscosity (mm^2/s)	
				40 °C	60 °C
DI water	7	0.998	0	0.652	0.452
WMEG	6.9	1.083	4.622	1.963	1.337
WGlycerol	5.9	1.138	4.068	2.976	1.806
WPEG	6.2	1.086	14.107	3.812	2.361
WPAG	6.4	1.051	9.202	7.907	2.957

Electrochemical tests were carried out in a Gamry Instruments Reference 600 Potentiostat (Warminster, PA, USA) according to the ASTM G3-14 standard with a three-electrode cell set up [37]. Round AISI 52100 steel 3.175 cm in diameter samples were ground up to 1200 grit using SiC paper and then exposed to the electrolyte as the working electrode (WE) with an exposed area of 3.14 cm^2, a graphite rod as the counter electrode (CE), a saturated calomel electrode (SCE) acting as a reference electrode (RE), and the different WBLs at room temperature (25 °C) as the electrolytes. First, open circuit potential (OCP) was monitored for 1800 s to stabilize the corrosion potential (E_{corr}). Linear polarization resistance (LPR) tests were performed within a potential range of ± 20 mV_{OCP} and scan rate of 0.125 mV/s according to ASTM G59-97 [38]. EIS measurements were conducted at the E_{corr}, in a frequency range between 10^{-2} and 10^5 Hz, a 10 mV rms excitation signal, and a step rate of 10 points per decade. Potentiodynamic polarization curves were performed in a potential range of +800 to -200 mV_{OCP} with a scan rate of 1.667 mV/s. All experiments were performed in triplicate.

The polarization resistance (R_p) was obtained from linear polarization resistance measurements by applying a small potential perturbation around the corrosion potential (E_{corr}). In this near-equilibrium region, the current-potential relationship can be approximated as linear, and the polarization resistance is defined as the slope of the potential-current response [39,40]:

$$R_p = \left(\frac{dE}{di}\right)_{E=E_{corr}} \quad (1)$$

where E is the electrode potential and i is the current density. The value of R_p was determined by performing a linear regression of the measured current-potential data within a narrow potential range around E_{corr}.

Potentiodynamic polarization curves were used to determine the corrosion potential (E_{corr}), corrosion current density (i_{corr}), and the anodic and cathodic Tafel slopes (β_a and β_c).

These slopes were obtained by fitting the linear regions of the anodic and cathodic branches of the polarization curves according to the Tafel relationship [41]:

$$\eta = \beta \log\left(\frac{i}{i_{corr}}\right) \tag{2}$$

where η is the overpotential, i is the current density, and β represents the anodic (β_a) or cathodic (β_c) Tafel slope expressed in V/dec.

The corrosion current density was estimated using the Stern–Geary relationship:

$$i_{corr} = \frac{B}{R_p} \tag{3}$$

where the Stern–Geary constant B is defined as follows [38,39]:

$$B = \frac{\beta_a \beta_c}{2.303(\beta_a + \beta_c)} \tag{4}$$

Here, i_{corr} is expressed in A/cm^2, R_p in Ω, and the Tafel slopes in V/dec. This methodology allows quantification of corrosion kinetics by combining LPR-derived polarization resistance with Tafel parameters obtained from potentiodynamic polarization measurements.

The final surfaces before and after testing had an average surface roughness of R_a = 0.029 ± 0.008 µm and R_a = 0.046 ± 0.014 µm, respectively, as can be seen in Figure 1.

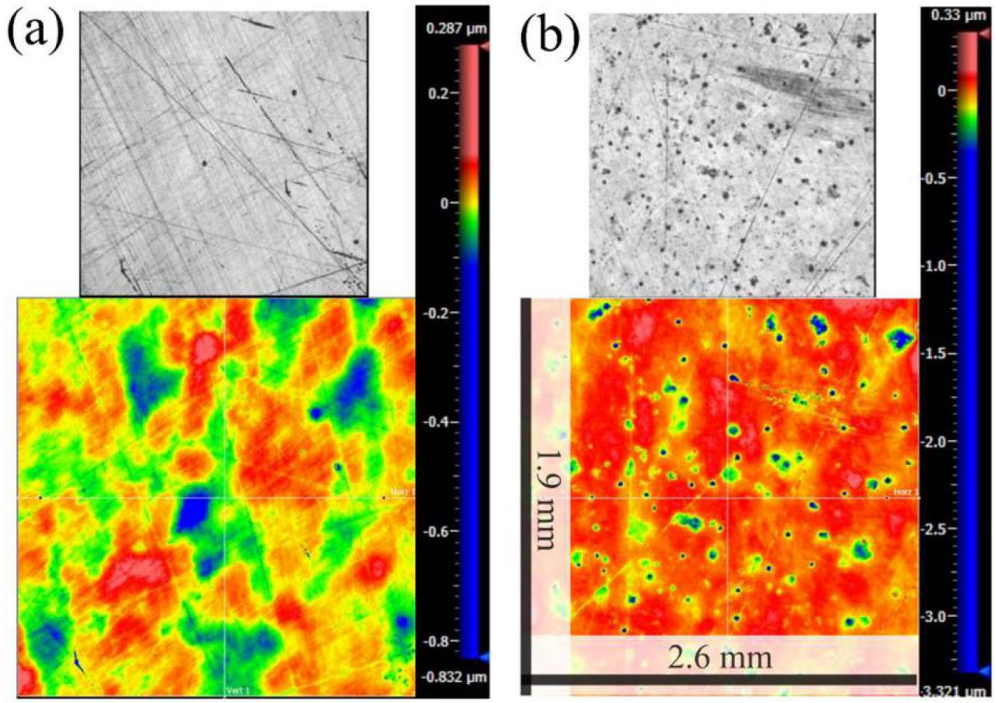


Figure 1. Surface topography of the samples: (**a**) pre-test, (**b**) after corrosion tests.

The electrical conductivity of the WBLs was evaluated using an Apera Instruments PC800 (Columbus, OH, USA) pH/Conductivity Meter equipped with a conductivity probe used to measure the conductivity of the aqueous solutions. A two-point calibration was performed using an 84 µS/cm standard buffer solution and a 1413 µS/cm standard buffer solution. Each fluid was measured at 23 °C ± 1 °C with three replicate measurements per fluid, reported as mean ± standard deviation.

Optical images of the exposed surface area of the AISI 52100 samples were taken with an optical microscope (OM) from Nikon Eclipse MA 100 (Melville, NY, USA). Anal-

ysis of the surfaces was performed using a scanning white-light interferometry (SWLI) microscope, Zygo NewView 9000 (Middlefield, CT, USA). Scanning electron microscopy (SEM) characterization and local composition analysis was performed via energy dispersive X-ray spectroscopy (EDX) using an FEI Quanta 200 microscope (Hillsboro, OR, USA). An acceleration voltage of 20 kV and a working distance of 10 mm were used according to the ASTM E986-04 standard [42].

3. Results

The open circuit potential (OCP) of the steel specimens was monitored as a function of immersion time in the different test fluids to evaluate the initial electrochemical response and surface stabilization behavior. OCP measurements provide insight into the thermodynamic tendency for corrosion and the establishment of equilibrium conditions at the metal–electrolyte interface prior to polarization testing. Figure 2a presents the evolution of the OCP with time for each fluid, along with the average steady-state potentials and associated standard deviations obtained after stabilization, as shown in Figure 2b. Monitoring the OCP allows assessment of how the different fluid chemistries influence surface activity and the formation of protective or reactive surface films before further electrochemical characterization.

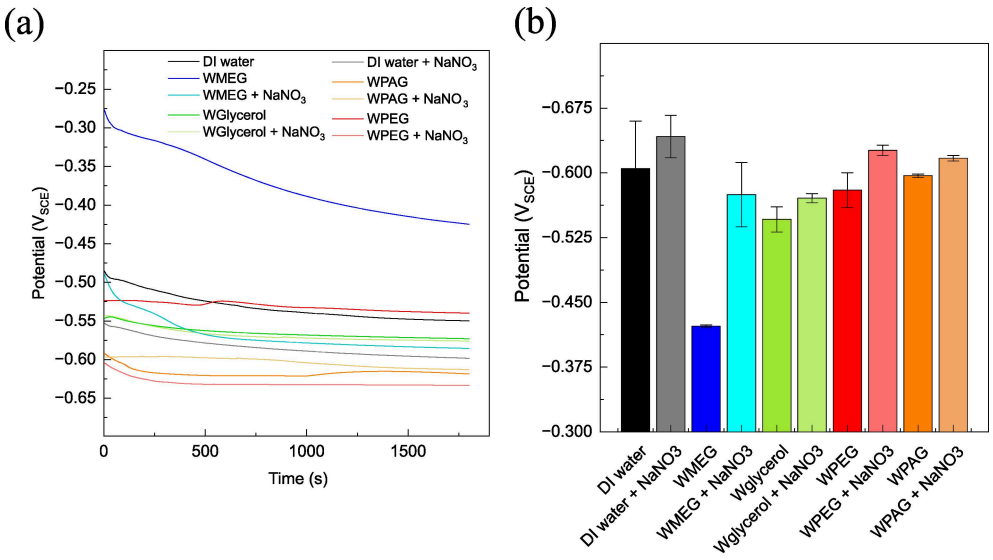


Figure 2. (**a**) Open circuit potential over time of the different solutions in AISI 52100 steel. (**b**) Average OCP values.

Potentiodynamic polarization curves obtained for the steel specimens in the different test fluids are shown in Figure 3. The curves exhibit the typical anodic and cathodic branches associated with electrochemical reactions occurring at the metal–electrolyte interface. Differences in both the corrosion potential (E_{corr}) and current density (i) are observed among the tested fluids, indicating that the chemical composition of the environment significantly influences the electrochemical response of the surface. In deionized (DI) water, the addition of $NaNO_3$ results in a slight reduction in the magnitude of the current response, suggesting improved corrosion resistance. In contrast, for the water-based lubricants (WBLs), the presence of $NaNO_3$ leads to higher corrosion current densities (i_{corr}) and a shift of E_{corr} toward more negative values, indicating an increase in electrochemical activity compared to the uninhibited systems.

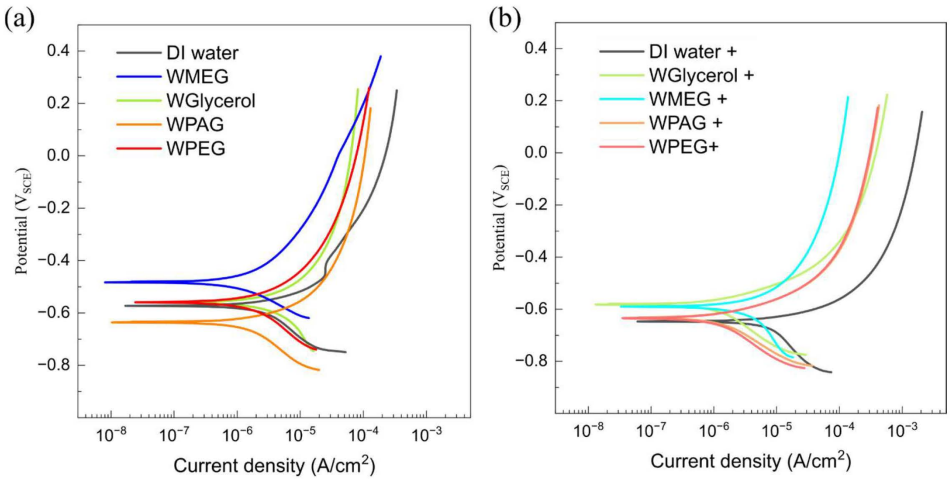


Figure 3. Potentiodynamic polarization curves for the different lubricant solutions: (**a**) No corrosion inhibitors, and (**b**) $NaNO_3$ inhibitor.

The Nyquist plots for AISI 52100 exposed to all fluids are presented in Figure 4. The plot shows differences in the electrochemical behavior of fluids. These differences are quantified after analyzing the Nyquist data and fitting the appropriate electrical equivalent circuit to each data set to better understand the processes occurring at the interfacial level.

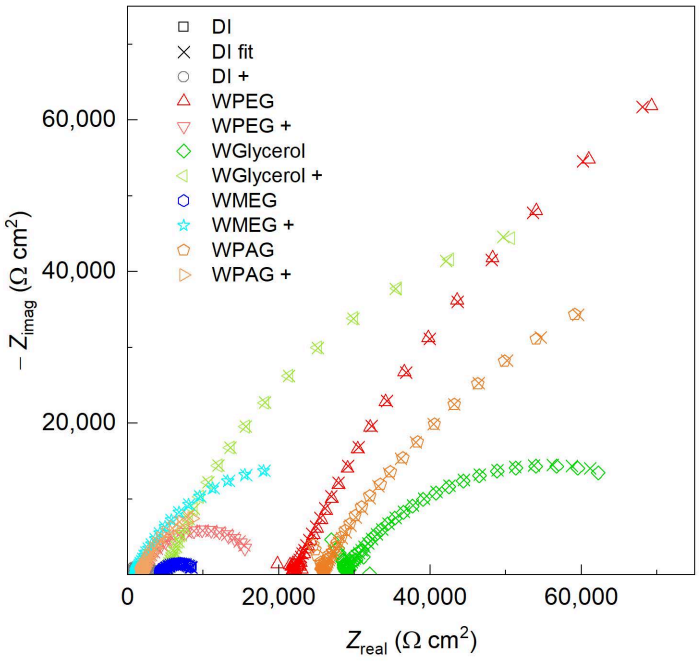


Figure 4. Nyquist plots of all fluids tested in AISI 52100 steel.

Representative optical images of the steel surfaces after electrochemical testing in the different fluids are shown in Figure 5. Clear differences in surface appearance are observed depending on the lubricant chemistry and the presence of the corrosion inhibitor. The specimen exposed to DI water exhibits significant surface discoloration and corrosion products, consistent with the higher corrosion current densities measured in the electrochemical tests. In contrast, the surfaces tested in the water-based lubricant formulations generally show reduced visible corrosion damage, with smoother and more uniform surface appearances. In particular, the glycerol- and PEG-based systems, which exhibited the lowest corrosion current densities and highest polarization resistance values, display comparatively minor surface degradation. When $NaNO_3$ is added, changes in the surface morphology become

evident in several of the lubricant systems, with increased discoloration and localized corrosion features observed in some samples. These visual observations qualitatively reflect the trends observed in the polarization measurements.

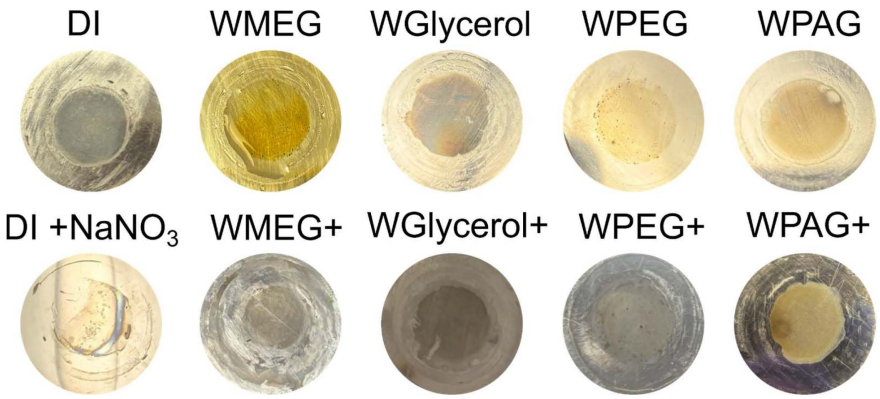


Figure 5. Optical images of the corroded specimens after all the tests.

4. Discussion

The electrochemical corrosion parameters were determined from open circuit potential (OCP), linear polarization resistance (LPR), potentiodynamic polarization measurements, and EIS. Prior to polarization measurements, the working electrode was allowed to stabilize at open circuit potential for 1800 s to reach a steady-state electrochemical condition.

Figure 2 shows the evolution of the open circuit potential (OCP) as a function of time for the different fluids, along with the average steady-state OCP values and associated standard deviations. In all cases, the potential exhibits an initial transient before stabilizing, which is typical of surface equilibration and the formation of surface films upon immersion. The WMEG electrolyte displays the most positive OCP values, indicating a more noble electrochemical behavior. In contrast, the WPEG+ (with corrosion inhibitor) solution shifts the potential toward more negative values, suggesting a more active surface condition consistent with a more aggressive electrolyte environment. The rest of the water-based lubricant formulations exhibit intermediate OCP values, indicating partial stabilization of the surface compared to the blank condition. Once stabilized, the potentials remain relatively constant, and the small standard deviations observed in the averaged values indicate good repeatability of the measurements. Overall, the results suggest that the different fluid chemistries influence the electrochemical state of the surface, with more negative potentials corresponding to a greater tendency toward active corrosion behavior.

The electrochemical parameters summarized in Table 3 reveal clear differences in the corrosion behavior of AISI 52100 steel depending on the chemistry of the water-based lubricant. Among the uninhibited fluids, DI water exhibited the highest corrosion current density ($i_{corr} = 19.85\ \mu A/cm^{-2}$), indicating the most aggressive corrosion environment. In contrast, the organic water-based mixtures significantly reduced the corrosion rate. In particular, WGlycerol and WPEG displayed the lowest i_{corr} values (0.79 and 0.85 $\mu A/cm^{-2}$, respectively) and the highest polarization resistance values ($R_p \approx 3.1 \times 10^4$ and $3.3 \times 10^4\ \Omega$), suggesting improved corrosion resistance relative to the other fluids. WMEG and WPAG exhibited intermediate behavior, with corrosion currents approximately one order of magnitude lower than DI water but higher than the glycerol- and PEG-based systems. These trends indicate that the chemical structure of the water-soluble organic components plays a significant role in moderating the electrochemical reactivity of the steel surface. Polyols such as glycerol and PEG are known to interact with metal surfaces and can reduce corrosion rates through adsorption and modification of the interfacial water structure, which can suppress both anodic dissolution and cathodic reactions.

Table 3. E_{corr} and i_{corr} parameters obtained via CPP of AISI 52100 samples in the different fluids.

Specimen	i_{corr} (μA/cm^2)	E_{corr} (V_{SCE})	β_a (V/dec)	β_c (V/dec)	R_p (Ω)
DI Water	19.85 ± 0.42	−0.621 ± 0.005	0.103 ± 0.008	0.406 ± 0.007	1313 ± 28
WMEG	3.16 ± 0.25	−0.580 ± 0.003	0.406 ± 0.082	0.226 ± 0.001	8275 ± 646
WGlycerol	0.79 ± 0.01	−0.609 ± 0.009	0.064 ± 0.002	0.105 ± 0.002	32,600 ± 210
WPEG	0.85 ± 0.01	−0.631 ± 0.002	0.109 ± 0.005	0.128 ± 0.007	30,650 ± 50
WPAG	2.11 ± 0.09	−0.617 ± 0.005	0.066 ± 0.007	0.109 ± 0.025	12,335 ± 515
DI Water + $NaNO_3$	17.13 ± 0.23	−0.633 ± 0.002	0.114 ± 0.006	0.384 ± 0.009	1521 ± 21
WMEG + $NaNO_3$	3.229 ± 0.05	−0.557 ± 0.005	0.069 ± 0.001	0.089 ± 0.006	8070 ± 120
WGlycerol + $NaNO_3$	2.14 ± 0.01	−0.564 ± 0.004	0.068 ± 0.005	0.086 ± 0.020	12,150 ± 50
WPEG + $NaNO_3$	4.6 ± 0.01	−0.587 ± 0.003	0.072 ± 0.012	0.176 ± 0.075	5664 ± 19
WPAG + $NaNO_3$	4.05 ± 0.07	−0.573 ± 0.012	0.092 ± 0.004	0.235 ± 0.026	6435 ± 112

The results obtained were compared to the available literature. A study of 50 wt.% ethylene glycol dilutions showed corrosion current densities of 0.31 μA/cm^2 for 4130 steel in 100 ppm NaCl, values similar to the ones obtained in the current study [43]. Another study on glycerol indicated corrosion current densities in the range 5 to 8 μA/cm^2 for a solution containing 2 wt.% NaCl [28]. A study in PEG showed the corrosion behavior of pure iron in water–PEG mixtures with corrosion current densities in the range 5 to 8 A/cm^2 [44]. Santambrogio et al. studied the corrosion behavior for electrolytes comprised of ethylene glycol with different acids with corrosion current densities ranging from 14 to 55 μA/cm^2 for low carbon steel [31]. All of the literature results are well within the range of the corrosion current densities observed in this study, despite the different alloys and electrolyte compositions.

The observed influence of glycol chemistry on corrosion behavior is consistent with previous studies of aqueous glycol systems used in automotive cooling applications. Water–ethylene glycol mixtures are known to alter electrochemical reactions at steel surfaces by modifying electrolyte conductivity, oxygen solubility, and interfacial adsorption behavior [25,26,45]. In cooling systems, corrosion inhibitors such as nitrates or nitrites are commonly used to promote the formation of protective oxide films and reduce anodic dissolution of steel components. However, the effectiveness of these inhibitors depends strongly on the surrounding electrolyte composition and the presence of competing species that may influence adsorption and film stability. The results obtained in this work suggest that similar interactions occur in water-based lubricants, where organic components such as glycols and polyols modify the metal–electrolyte interface and influence corrosion kinetics.

The addition of $NaNO_3$ altered the electrochemical response of the systems, although the effect was not uniform across the different fluids. While the inhibitor slightly reduced the corrosion current density in DI water, its presence generally increased i_{corr} and reduced polarization resistance in several of the water-based lubricant formulations, particularly in the PEG- and PAG-based mixtures. For example, the corrosion current density of WPEG increased from 0.85 to 4.6 μA/cm^2 after the addition of $NaNO_3$, accompanied by a substantial decrease in R_p. Nitrate salts are commonly used as corrosion inhibitors in aqueous systems because they can promote the formation of protective ferric oxide or hydroxide films on steel surfaces and shift the corrosion potential toward more noble values [46]. However, the effectiveness of such inhibitors strongly depends on the surrounding electrolyte composition and the presence of other adsorbing species. In complex aqueous-organic systems such as the WBL formulations studied here, organic molecules and glycol-based components may compete with nitrate species for adsorption sites or alter oxide film stability, thereby modifying the inhibition mechanism. Additionally, increased ionic strength and conductivity in multi-component fluids can enhance charge transfer processes and accelerate electrochemical reactions. Changes in the corrosion potential (E_{corr}) further indicate that

$NaNO_3$ influences the balance between anodic dissolution and cathodic reduction reactions rather than producing a simple passivating shift.

The different behavior of $NaNO_3$ in the WBL formulations may be related to interactions between nitrate species and the organic components of the fluid. Glycols and polyols are known to adsorb on steel surfaces and modify the metal–electrolyte interface, potentially competing with nitrate ions for adsorption sites and altering passive film stability [47,48]. In addition, changes in electrolyte conductivity and interfacial water structure in aqueous-organic mixtures can influence charge-transfer reactions and corrosion kinetics [40,49]. Overall, these results demonstrate that corrosion behavior in water-based lubricants is strongly dependent on base fluid chemistry and that the effectiveness of nitrate-based inhibition strategies must be evaluated within the specific fluid environment.

Before performing the EIS analysis, Kramers–Kronig (KK) transforms were produced to determine the robustness of the data. The analysis consists of calculating the real impedance values using the imaginary experimental data and vice versa. In order to determine the robustness of the experimental data, both results, experimental and calculated data, must have a good correlation [50,51]. This can be seen in Figure 6, where the empty symbols represent the experimental values and the crosses represent the calculated values; the overlapping indicates a good fit, thus showing the robustness of the data obtained. For clarity and compactness only the results for the WMEG test are shown.

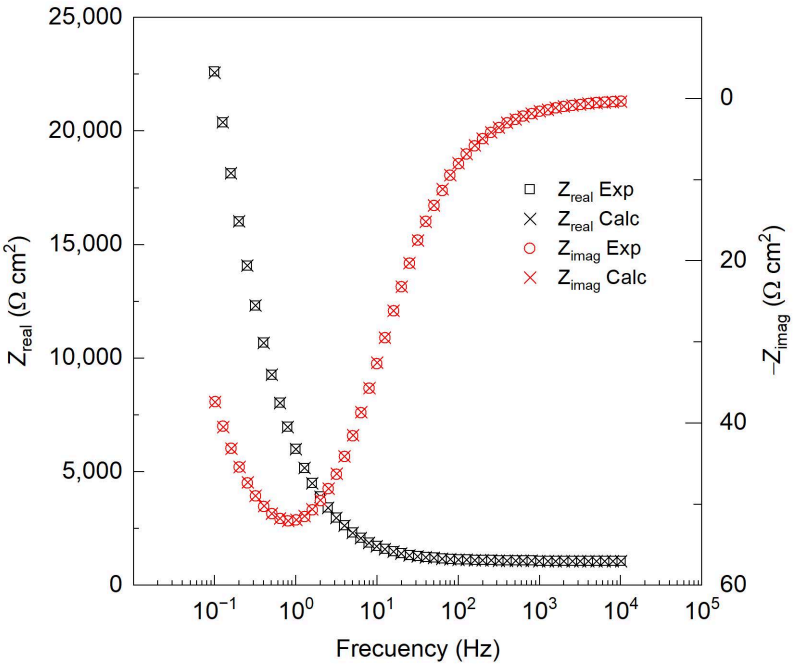


Figure 6. Kramers–Kronig (KK) transforms of AISI 52100 steel tested in WMEG fluid.

The EIS Nyquist plots are presented in Figure 4 for the AISI 52100 steel in the different WBL fluids. The proposed electrical equivalent circuit (EEC) used to fit the EIS data is shown in Figure 7. The EEC presents a hierarchically distributed equivalent circuit consisting of the following: R_s, the resistance of the solution (this is attributed to the ohmic resistance between the WE and the RE); CPE_{dl} which is the constant phase element related to the double layer (low frequencies); and R_{ct} which is the charge transfer resistance (presenting an inverse proportionality with the corrosion rate). This EEC proposal is supported by observing the Bode plots in Figure 8. The Bode phase plots (Figure 8) show a single broad phase maximum, indicating that the corrosion response is dominated by one principal relaxation process associated with the electrochemical interface [51,52]. Minor

deviations in the phase angle slope are observed at high frequencies; however, these are attributed to interfacial non-idealities or measurement artifacts rather than a distinct second time constant. Specifically, for the WGlycerol and WPAG fluids which exhibit a minor deviation at low frequencies that could suggest a secondary process, the attempts to fit the data with a two-time-constant equivalent circuit yielded a goodness of fit of ~10^{-3} with parameter errors exceeding 40%, indicating an over-parameterized model. The single R_s–(CPE//R_{ct}) circuit was therefore retained for all fluids, with the low-frequency deviation in WGlycerol attributed to measurement non-stationarity during the extended acquisition window. Therefore, the selected R_s–R_{ct}//CPE_{dl} circuit adequately describes the system without introducing additional elements [53]. In the time constant associated with the double layer, the *CPE* element represents a branched ladder *RC* network that is presented instead of an ideal capacitor due to the non-ideal capacitance of an electrode in an active state [50]. The impedance of this *CPE* can be obtained by $Z_{\mathrm{CPE}} = (Y)^{-1}(\mathrm{j}\omega)^{-n}$, where Y is the admittance (S cm^{-2} s^{n}), ω is the angular frequency (rad s^{-1}), j is the imaginary number, $\mathrm{j}^2 = (-1)$, and n is a dimensionless fraction exponent ranging from −1 to 1. The fitting parameters of the Nyquist plots using the proposed EEC are presented in Table 4. The goodness of fit (χ^2) for all the alloys tested falls within 10^{-4}, and the error percentage for each parameter is always below 10% for all the tests performed.

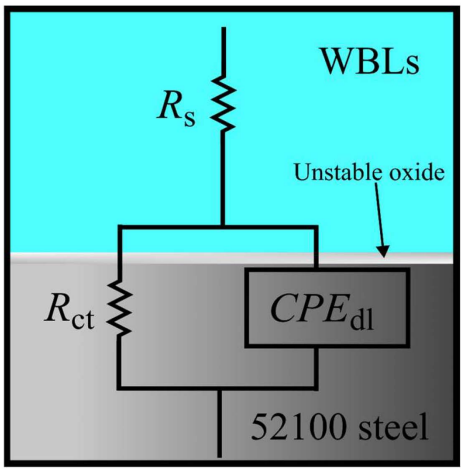


Figure 7. Proposed electrical equivalent circuit for the EIS tests.

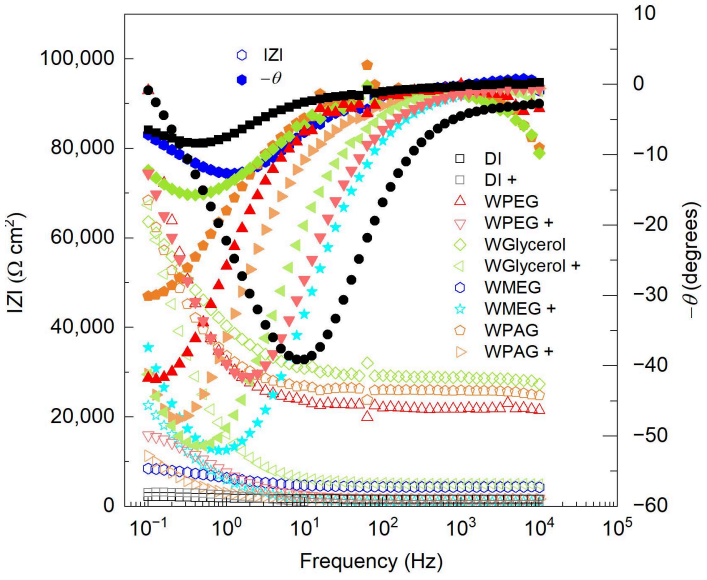


Figure 8. Bode plots for AISI 52100 in all tested fluids.

Table 4. EIS fitting parameters of AISI 52100 steel submerged in the different WBLs.

Specimen	R_s Ω cm^2	R_{ct} Ω cm^2	Y_{dl} S/cm^2 s^{n,dl}	n_{dl}	$C_{eff,dl}$ μF/cm^2
DI Water	313.8	197.04	4.15×10^{-3}	0.63	2.75×10^{-3}
DI Water + $NaNO_3$	68.36	582.8	2.52×10^{-4}	0.77	7.30×10^{-5}
WMEG	860.8	1007.6	4.16×10^{-4}	0.67	1.87×10^{-4}
WMEG + $NaNO_3$	211.8	8348	2.19×10^{-4}	0.75	7.98×10^{-5}
WGlycerol	5696	10,912	8.93×10^{-5}	0.62	4.59×10^{-5}
WGlycerol + $NaNO_3$	994.8	27,960	8.54×10^{-5}	0.78	4.19×10^{-5}
WPEG	4366	65,800	7.99×10^{-5}	0.73	5.26×10^{-5}
WPEG + $NaNO_3$	342.4	3288	1.47×10^{-4}	0.79	6.49×10^{-5}
WPAG	5098	30,840	1.15×10^{-4}	0.68	8.27×10^{-5}
WPAG + $NaNO_3$	330.4	6288	5.91×10^{-4}	0.76	3.43×10^{-4}

From the fitting values presented in Table 4, some trends can be extracted; R_s presents an average value on the order of 10^3 Ω cm^2, with variations depending on electrolyte composition. The R_{ct} varies significantly between samples, ranging from 10^3 to 10^5 Ω cm^2, reflecting substantial differences in corrosion resistance among the tested fluids. The effect of $NaNO_3$ is not uniform across all systems. In DI water and water–glycerol solutions, the addition of $NaNO_3$ increases $R_{ct,}$ indicating improved corrosion resistance. In contrast, for PEG- and PAG-based lubricants, the addition of $NaNO_3$ leads to a decrease in R_{ct}, suggesting a deterioration of the protective behavior. The Y_{dl} remains in the range of 10^{-6} to 10^{-4} S/cm^2 s^{n,dl}, for the whole set of lubricants. The n_{dl} values range from 0.62 to 0.79, indicating that the interface shows a non-ideal capacitor behavior, which is influenced by the applied polarization, the surface roughness, the presence of defects, and the presence of oxide films or adsorbed species.

The electrical conductivity of all the tested fluids is presented in Table 5. Among the neat WBLs, the conductivity ranged from 1.9 μS/cm (WPAG) to 62.9 μS/cm (WGlycerol), with WPAG falling below DI water (6.2 μS/cm), reflecting differences in ionic dissociation behavior across the fluid chemistries. The addition of $NaNO_3$ increased the conductivity by one to three orders of magnitude across all fluids, with DI+ reaching the highest value (3213 μS/cm) and WPAG+ the most moderate increase among the inhibited polymer fluids (264 μS/cm). These conductivity values are consistent with the solution resistance (R_s) values extracted from EIS fitting (Table 4), providing independent validation of the electrochemical measurements.

Table 5. Average and standard deviation of conductivity for tested fluids.

Specimen	Average Conductivity (μS/cm)	STD
DI Water	6.24	0.01
DI Water + $NaNO_3$	3213.33	20.09
WMEG	27.40	0.03
WMEG + $NaNO_3$	941.33	1.35
WGlycerol	62.87	0.24
WGlycerol + $NaNO_3$	156.80	0.78
WPEG	55.30	0.15
WPEG + $NaNO_3$	597.30	0.58
WPAG	1.88	0.05
WPAG + $NaNO_3$	253.33	0.96

A mechanistic interpretation can be proposed based on the evolution of R_{ct}, Y_{dl}, and n_{dl}. In DI water, the low R_{ct} and high Y_{dl} indicate an active corrosion process with a thin and poorly protective oxide layer. The addition of $NaNO_3$ reduces Y_{dl} and increases

n_{dl} suggesting the formation of a more homogeneous and stable interfacial film, likely associated with enhanced passivation and suppression of active dissolution.

In water–glycerol systems, a strong synergistic effect is observed. Glycerol molecules can adsorb at the steel/electrolyte interface and structure the interfacial region through hydrogen bonding, partially blocking active sites. When $NaNO_3$ is added, R_{ct} increases by more than one order of magnitude, while n_{dl} approaches more ideal capacitive behavior. This suggests the formation of a compact and protective interfacial layer combining organic adsorption and improved surface passivation [28,30,31,43,44,54].

In contrast, for PEG- and PAG-based lubricants, high R_{ct} values are already observed without inhibitor, indicating that these polymers form an effective barrier layer at the interface. The addition of $NaNO_3$ results in a decrease in R_{ct} and an increase in Y_{dl}, which can be attributed to competitive adsorption or disruption of the polymer-rich boundary layer [43]. The presence of nitrate ions and increased ionic conductivity may facilitate charge transfer by creating conductive pathways through the organic film.

For WMEG systems, intermediate behavior is observed, where the addition of $NaNO_3$ slightly modifies the interfacial structure (as indicated by changes in Y_{dl} and n_{dl}) but does not significantly improve R_{ct}. This suggests that MEG provides partial surface coverage, but the interaction with nitrate does not produce a strong synergistic or detrimental effect [54].

In order to correct the value of the pseudo-capacitance of the double-layer (Y_{dl}) and find the effective capacitance ($C_{eff,dl}$), the R_s and R_{ct} are considered and used in combination with the Y_{dl} and n_{dl}. The equation proposed by Brug et al. was used to calculate $C_{\mathrm{eff,dl}}$ (see Equation (5)) [55–57]:

$$C_{eff,dl} = \left[Y_{dl} \left(\frac{1}{R_s} + \frac{1}{R_{ct}} \right)^{(n_{dl}-1)} \right]^{\frac{1}{n_{dl}}} \quad (5)$$

Using Equation (5), the following $C_{eff,dl}$ values are obtained and shown in Figure 9. In addition, the R_{ct} values are also included to compare the evolution of both parameters with each thermomechanical treatment. From Figure 9, an inverse relationship between $C_{eff,dl}$ and R_{ct} is observed across all fluids. Systems with higher R_{ct} exhibit lower $C_{eff,dl}$, indicating the formation of more protective interfacial films. This trend confirms that improved corrosion resistance is associated with reduced effective double-layer capacitance, which reflects decreased active surface area and/or increased film thickness. The higher the R_{ct}, the lower the $C_{eff,dl}$, which corroborates the previous results as the higher the impedance and the lower the capacitance the more protection the film imparts [50,58,59]. Overall, the combined EIS analysis suggests that corrosion protection in these water-based lubricants is governed by the interplay between inorganic passivation (promoted by nitrate ions) and organic adsorption layers (provided by glycerol, PEG, and PAG) [27–31]. The effectiveness of $NaNO_3$ depends strongly on the base fluid chemistry, leading to either synergistic enhancement (DI and glycerol systems) or competitive/interfering effects (PEG and PAG systems). These findings are in accordance with previous literature results [31].

The optical images provide qualitative confirmation of the electrochemical trends obtained from the polarization experiments. The severe surface discoloration and corrosion products observed on the specimen exposed to DI water are consistent with the high corrosion current density measured for this fluid, indicating significant metal dissolution. The yellow-brown coloration visible on several samples is characteristic of iron oxide and oxyhydroxide corrosion products such as Fe_2O_3 and FeOOH, which commonly form during the corrosion of steel in aqueous environments [60,61]. In contrast, the relatively uniform surfaces observed for the glycerol- and PEG-based fluids agree with the lower corrosion currents and higher polarization resistance values, suggesting that these

organic components help reduce electrochemical activity at the steel interface. Organic molecules such as polyols and glycols can adsorb onto metal surfaces and modify the interfacial chemistry, reducing both anodic dissolution and cathodic reduction reactions and thereby decreasing the overall corrosion rate [47,48]. In the systems where $NaNO_3$ increased the corrosion current density, the optical images reveal more pronounced surface changes and localized corrosion features, supporting the interpretation that the inhibitor does not provide effective protection in these complex aqueous-organic environments. The performance of nitrate-based inhibitors is known to depend strongly on electrolyte composition and oxide film stability, and their protective effect may be disrupted when competing species modify adsorption processes at the metal surface [40,46]. Overall, the surface observations align well with the electrochemical measurements, indicating that the corrosion behavior inferred from the polarization data is consistent with the physical condition of the tested surfaces.

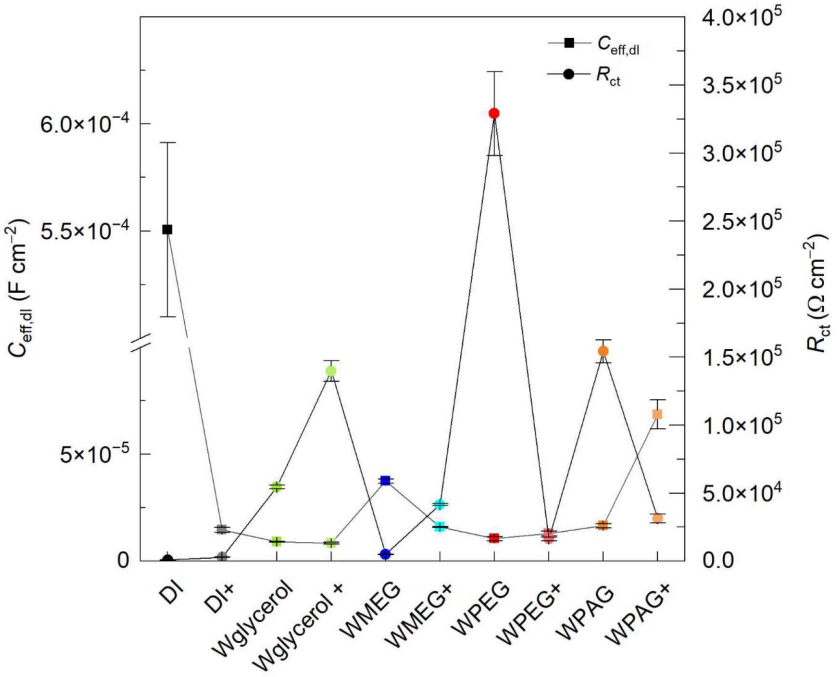


Figure 9. Evolution of $C_{eff,dl}$ and R_{ct} parameters.

SEM micrographs and EDAX compositional analysis were performed on representative ball specimens to corroborate the electrochemical findings and characterize the surface degradation morphology (Figure 10 and Table 6, respectively). The O:Fe ratio, derived from EDAX area scans, is used as the primary indicator of the surface oxidation state; carbon values are reported as indicative only, as contributions from the carbon-based mounting adhesive cannot be fully excluded from broad-area scans. The SEM micrographs reveal distinct surface morphologies that are consistent with the electrochemical behavior observed in the EIS analysis. In DI water, the corroded surface exhibits the most severe morphological damage, characterized by widespread pitting and a rough, heterogeneous topography across the exposed surface (Figure 10). EDAX confirms the highest C and O weight fractions (27.27 and 14.42 wt.%, respectively) and the lowest Fe content (55.63 wt.%) among all fluids tested, yielding the highest O:Fe ratio of up to 0.36, indicative of substantial oxide accumulation at corrosion sites, consistent with the lowest R_{ct} value obtained from EIS, confirming active and largely unimpeded corrosion in the absence of any organic additive or inhibitor. EDAX shows the presence of an oxygen-containing surface layer whose composition is consistent with a thin iron oxide/oxyhydroxide film, although phase

identification requires complementary techniques such as Raman spectroscopy or XPS. In contrast, the WGlycerol surface appears considerably smoother and more uniform, with only minor surface features visible and a significantly reduced O content (2.56 wt.%) and elevated Fe (87.9 wt.%), pointing to a cleaner metallic surface with minimal oxide buildup, in agreement with the high R_{ct} observed for this fluid. The WMEG surface shows an intermediate response, with a localized bright region visible in the micrograph that is characteristic of a non-uniform corrosion product deposit, while the EDAX composition (C: 11.32, O: 2.49, Fe: 84.00 wt.%) suggests a partially protected surface. The WPEG surface displays a relatively featureless morphology with low O (2.81 wt.%) and high Fe (87.39 wt.%), suggesting that the PEG polymer effectively suppresses corrosive attack at the steel/electrolyte interface, corroborated by the highest R_{ct} (65,800 Ω cm^2) of all fluids tested. The WPAG surface similarly shows clean metallic morphology with minimal corrosion products and the lowest O:Fe ratios (0.02) recorded across the entire dataset (0.022–0.033) and a high R_{ct} of 30,840 Ω cm^2, reinforcing the conclusion that PAG provides a significant effective interfacial barrier [31]. Across all glycol and polymer-based fluids, the consistently low O:Fe ratios, well below the theoretical stoichiometry of even the least oxidized iron oxide phase, indicate that the EDAX signal is dominated by the metallic iron substrate, reflecting the nm-scale thickness of the surface oxide relative to the µm-scale interaction volume of the electron beam, and further confirming that the corrosion products form only a thin, discontinuous film rather than a developed oxide layer. Upon addition of $NaNO_3$, the surface morphologies change markedly in a fluid-dependent manner. DI+ surfaces retain significant surface degradation with general corrosion features, consistent with the moderate R_{ct} improvement observed. WGlycerol+ exhibits a notable increase in the number and uniformity of discrete pits distributed across an otherwise smooth surface, suggesting that while $NaNO_3$ promotes a more homogeneous passive film, consistent with the large R_{ct} increase, localized breakdown at inclusion sites still occurs. WMEG+ similarly shows a region with distributed pitting, consistent with the limited synergistic effect of $NaNO_3$ in MEG-based systems identified from EIS. Most strikingly, WPAG+ displays an entirely different morphology, with a surface covered by dark, irregularly distributed corrosion patches occupying a substantial fraction of the exposed area, with elevated C (35–61 wt.%) and O (8–11 wt.%) and dramatically reduced Fe (30–52 wt.%), the highest O:Fe ratios in the entire $NaNO_3$ dataset (0.22–0.27). This severe surface degradation directly corroborates the EIS finding that $NaNO_3$ decreases R_{ct} and increases Y_{dl} in the PAG system, consistent with disrupting the protective polymer boundary layer and exposing large areas of the steel surface to active corrosion. Taken together, the SEM and EDAX data consistently support a corrosion mechanism governed by a weak, non-passive interfacial oxide whose protective character is modulated by organic adsorption from the lubricant additives, with $NaNO_3$ producing divergent effects depending on the base fluid chemistry [27–29].

The corrosion of AISI 52100 steel in all water-based lubricants tested is governed by a single charge-transfer-controlled process at a weak, non-passive oxide interface, as evidenced by the single time constant in the EIS response. The native oxide film is insufficient to prevent either uniform or localized dissolution. Fluid additives modulate but do not eliminate the corrosion process: organic molecules (glycerol, PEG, PAG) adsorb at the interface and suppress general dissolution with varying intensities, shifting the corrosion mode toward localized pitting at heterogeneous sites (carbide inclusions, surface defects). $NaNO_3$ enhances passivation in simple aqueous systems but disrupts polymeric adsorption layers in PEG/PAG-based fluids, paradoxically promoting uniform attack [30–32]. The inverse R_{ct}–$C_{eff,dl}$ relationship across all systems confirms that corrosion protection is directly linked to the extent of active surface area suppression, whether through inorganic passivation or organic adsorption. Khomami et al. [45] investigated the electrochemical behavior of AISI

4130 steel in ethylene glycol–water mixtures and reported that the corrosion rate decreased consistently with increasing ethylene glycol concentration, attributed to the adsorption of glycol molecules at the steel surface and a reduction in the double-layer capacitance, a mechanism directly consistent with the reduced corrosion current densities and lower $C_{eff,dl}$ values observed in the present work for WMEG relative to DI water. Importantly, Khomami et al. [45] also found that while both nitrite and nitrate provided surface passivation, nitrate yielded lower inhibition efficiency than nitrite, and that the addition of these anions shifted E_{corr} in a manner dependent on their competitive adsorption against aggressive Cl^- ions, a behavior analogous to the fluid-dependent E_{corr} shifts and inconsistent inhibition response of $NaNO_3$ observed across the different WBL formulations in the present study. Khomami et al. [61] further showed through kinetic and thermodynamic analysis that the adsorption of inhibitor species on steel in ethylene glycol–water systems is a spontaneous process governed by competitive surface interactions, reinforcing the interpretation that in complex aqueous-organic environments, the effectiveness of inorganic inhibitors is strongly modulated by the pre-existing organic adsorption layer. Figure 11 shows the proposed corrosion mechanism for the different sets of fluids characterized according to their electrochemical response and which is in accordance with previously published data [43,54,62].

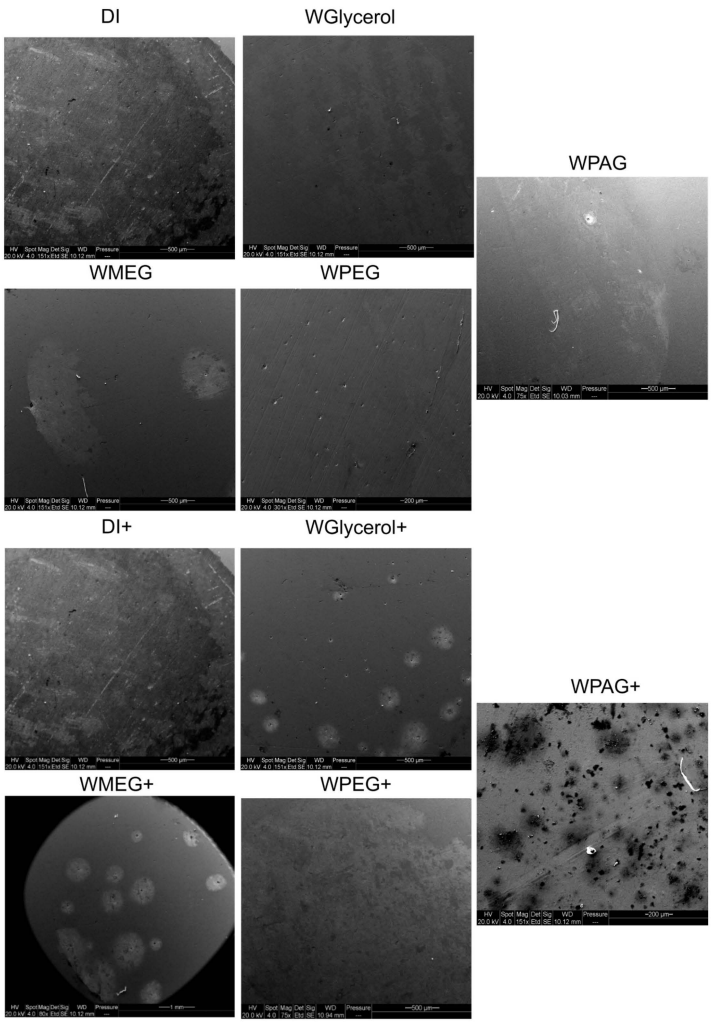


Figure 10. SEM micrographs and EDAX compositions of AISI 52100 steel specimens after electrochemical testing in WBLs.

Table 6. EDAX elemental composition (wt%) and O:Fe ratio of AISI 52100 steel specimens after electrochemical testing in plain WBLs and $NaNO_3$-containing WBLs. *Carbon values are reported as indicative only due to potential contributions from the carbon-based mounting adhesive during SEM specimen preparation.

Specimen	C (wt.%)	O (wt.%)	Cr (wt.%)	Fe (wt.%)	O:Fe
DI Water	27.27	14.42	2.68	55.63	0.26
DI Water + $NaNO_3$	29.21	15.42	2.79	52.58	0.29
WMEG	11.32	2.49	2.19	84.00	0.03
WMEG + $NaNO_3$	7.84	2.67	2.61	86.88	0.03
WGlycerol	7.72	2.56	1.82	87.9	0.03
WGlycerol + $NaNO_3$	12.83	2.79	2.31	82.07	0.03
WPEG	7.96	2.81	1.84	87.39	0.03
WPEG + $NaNO_3$	10.42	2.87	3.09	83.62	0.03
WPAG	5.91	2.21	2.00	89.87	0.02
WPAG + $NaNO_3$	60.50 *	8.12	1.06	30.32	0.27

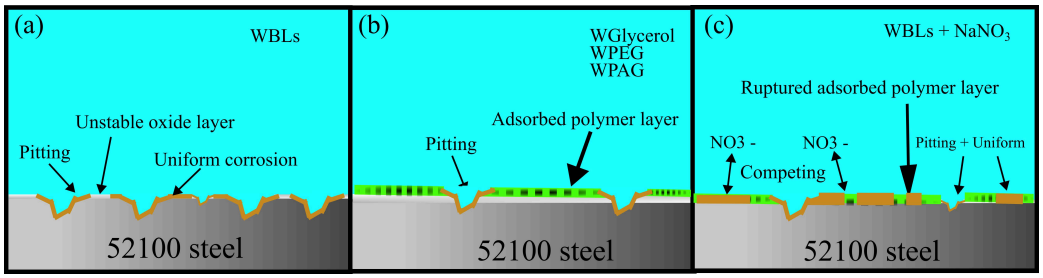


Figure 11. Proposed corrosion mechanism for the WBLs in AISI 52100 steel: (**a**) as-mixed WBLs display pitting and uniform corrosion, (**b**) Glycerol, PEG and PAG adsorb on the 52100 steel surface and mitigate uniform corrosion and slowcorrosion rates, and (**c**) addition of $NaNO_3$ promotes rupture of the adsorbed layer thorugh a competing mechanism, enhancing uniform corrosion.

White-light interferometry was employed in Figure 12 to characterize the post-test surface topography of all samples, providing direct three-dimensional corroboration of the proposed corrosion mechanism. The pit depth data in Table 7 reveal trends that are broadly consistent with the EIS and SEM/EDAX findings, although it should be noted that the measured values likely represent a lower bound of the true pit depth, as surface corrosion products and oxide films present on the corroded surfaces may partially fill or obscure pit cavities, hindering accurate depth measurement. Electrochemical etching of the corroded surfaces prior to interferometry would remove these products and provide a more accurate description of the actual pit morphology. With this caveat in mind, the data still reveal meaningful trends.

In DI water, the maximum pit depth of 5.18 µm reflects severe unimpeded corrosion, consistent with the lowest R_{ct} recorded, and decreases to 2.37 µm upon $NaNO_3$ addition, corroborating the nitrate-enhanced passivation observed electrochemically. WGlycerol exhibits one of the shallowest pit depths among uninhibited fluids (1.59 µm), consistent with partial surface blocking by glycerol adsorption. Yet $NaNO_3$ addition produces the deepest pit recorded across the entire dataset (5.61 µm), suggesting that while the average interfacial resistance increases, the remaining breakdown sites are attacked more aggressively. WMEG follows a similar detrimental trend upon inhibitor addition, with pit depth increasing from 3.69 to 5.19 µm. In contrast, WPEG and WPAG show shallow pits in their uninhibited forms (1.63 and 2.26 µm, respectively), and pit depths decrease further upon $NaNO_3$ addition (1.08 and 1.35 µm). This apparent contradiction with the reduced R_{ct} observed in EIS for these fluids is reconciled by considering that nitrate disrupts the polymer boundary layer and redistributes corrosive attack more uniformly across the surface, reducing individual pit depths while increasing the total corroded area, a transition from localized to combined localized and uniform corrosion that is directly visible in the interferometry images and

consistent with the SEM observations. Furthermore, the presence of oxide films on the more severely corroded surfaces may additionally contribute to an underestimation of pit depths in those specimens, meaning the relative differences between fluids reported here should be interpreted with caution. Collectively, the interferometry data confirm that corrosion severity and spatial distribution of attack are governed by the interplay between organic adsorption and inorganic passivation, as proposed in the mechanistic framework derived from the EIS analysis, while also highlighting the need for surface preparation protocols in future work to enable more quantitative pit depth characterization.

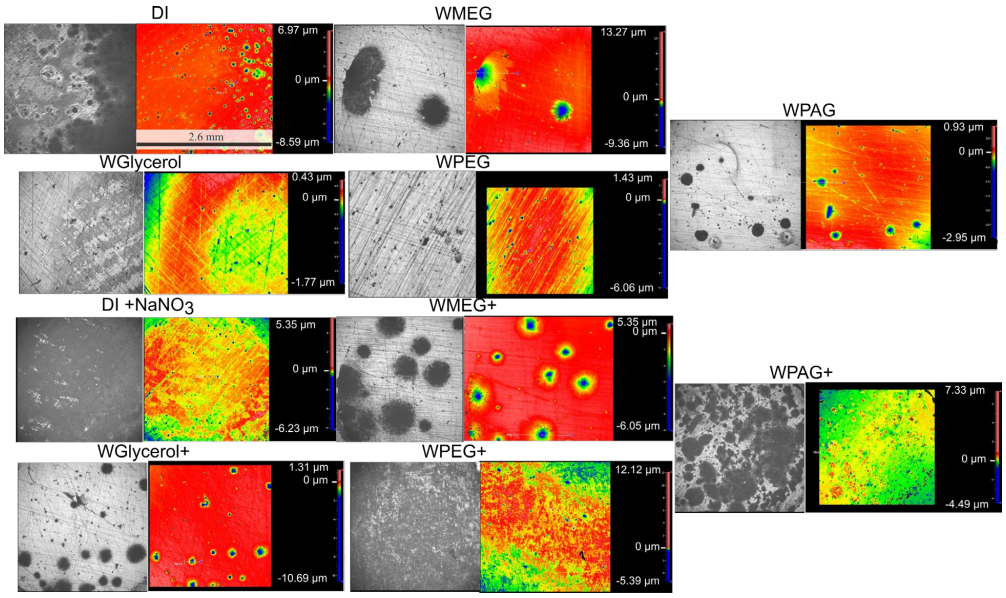


Figure 12. White-light interferometry of the AISI 52100 steel tested surfaces for all fluids.

Table 7. Average and standard deviation pit depths for the tested fluids.

Specimen	Max Pit Depth (µm)	STD (µm)
DI Water	5.18	0.97
DI Water + $NaNO_3$	2.37	0.54
WMEG	3.69	0.68
WMEG + $NaNO_3$	5.19	0.82
WGlycerol	1.59	0.46
WGlycerol + $NaNO_3$	5.61	0.78
WPEG	1.63	0.63
WPEG + $NaNO_3$	1.08	0.29
WPAG	2.26	0.34
WPAG + $NaNO_3$	1.35	0.44

5. Conclusions

This study evaluated the electrochemical corrosion behavior of AISI 52100 bearing steel in 50 wt.% aqueous mixtures of glycerol, MEG, PEG, and PAG, with and without $NaNO_3$ as a corrosion inhibitor. The following conclusions can be drawn.

The chemistry of the base fluid plays a dominant role in determining corrosion kinetics and surface stability. Among the uninhibited fluids, DI water exhibited the highest corrosion current density (19.85 µA/cm^2) and the lowest charge transfer resistance (197 Ω cm^2), confirming that pure aqueous environments promote rapid anodic dissolution of the steel surface. In contrast, glycerol- and PEG-based systems exhibited the lowest corrosion current densities (0.79 and 0.85 µA/cm^2, respectively) and the highest polarization resistance values (~3.1 × 10^4 and 3.3 × 10^4 Ω), indicating that the molecular structure of the organic

components significantly moderates electrochemical reactivity through adsorption-driven interfacial effects.

EIS analysis across all fluids revealed a single charge-transfer-controlled relaxation process, evidenced by a single broad phase maximum in the Bode plots, supporting the use of a single R_s–(CPE//R_{ct}) equivalent circuit. This single time constant response is consistent with a corrosion mechanism governed by a weak, non-passive oxide interface at the steel surface. Organic additives modulate but do not eliminate this process: glycerol, PEG, and PAG adsorb at the interface and suppress general dissolution with varying effectiveness, shifting the dominant corrosion mode from uniform attack toward localized pitting at heterogeneous sites such as carbide inclusions and surface defects. The inverse R_{ct}–$C_{eff,dl}$ relationship observed across all systems confirms that corrosion protection is directly linked to the suppression of active surface area, whether through inorganic passivation or organic adsorption.

The addition of $NaNO_3$ produced fluid-dependent effects that are mechanistically distinct across the tested systems. In DI water, nitrate addition slightly reduced corrosion activity through enhanced passivation. In glycerol-based systems, a strong synergistic effect was observed, with R_{ct} increasing nearly threefold upon inhibitor addition, attributed to the combined action of glycerol adsorption and nitrate-promoted surface passivation. In contrast, $NaNO_3$ was detrimental in PEG- and PAG-based systems, increasing corrosion current density and decreasing R_{ct}, which is attributed to competitive disruption of the established polymer boundary layer by nitrate ions and increased interfacial ionic conductivity. These findings demonstrate that nitrate-based inhibition strategies developed for simple aqueous systems cannot be directly transferred to complex aqueous-organic lubricant environments without accounting for the base fluid chemistry.

Surface characterization by SEM/EDAX and white-light interferometry corroborated the electrochemical results. EDAX confirmed the presence of a thin iron oxide/oxyhydroxide surface layer across all specimens, with O:Fe ratios well below the stoichiometry of any discrete iron oxide phase, consistent with a nm-scale oxide film dominated in the EDAX signal by the metallic iron substrate. Phase identification of the corrosion products would require complementary techniques such as Raman spectroscopy or XPS. White-light interferometry revealed fluid-dependent pit depth distributions broadly consistent with the EIS trends, although the measured values likely represent a lower bound of true pit depth due to partial infilling of pit cavities by corrosion products; electrochemical etching prior to surface measurement is recommended in future work for more accurate quantitative characterization.

Overall, these results confirm that the corrosion performance of water-based lubricants in contact with AISI 52100 steel is strongly governed by the interplay between organic adsorption from the base fluid and inorganic passivation promoted by inhibitor species. The fluid-dependent response to $NaNO_3$ underscores the need for inhibitor strategies tailored to specific lubricant chemistries. Future work combining tribocorrosion testing with the electrochemical framework established here would provide additional mechanistic insight into the coupled degradation behavior under dynamic contact conditions relevant to electrified drivetrain applications.

Author Contributions: Conceptualization, J.B.; methodology, J.B.; validation, J.B., E.K. and R.K.; formal analysis, J.B., E.K., K.Z.H. and R.K.; investigation, K.Z.H., E.K. and R.K.; resources, C.D. and J.B.; data curation, E.K., K.Z.H. and R.K.; writing—original draft preparation, J.B.; writing—review and editing, J.B., E.K., K.Z.H., R.K. and C.D.; visualization, J.B.; supervision, C.D.; project administration, C.D. and J.B.; funding acquisition, C.D. All authors have read and agreed to the published version of the manuscript.

Funding: This research was funded by The Timken Company, grant number AWD 000013.

Data Availability Statement: The data presented in this study are available on request from the corresponding author due to an ongoing study.

Acknowledgments: Authors would like to acknowledge The Timken company for their funding of this research. Furthermore, authors would like to acknowledge the students and staff at AETL and The University of Akron. Authors would like to thank Bill Wenzel from The University of Akron for his support preparing samples. Authors would like to thank BASF for providing the PAG samples.

Conflicts of Interest: The authors declare that this study received funding from The Timken Company. The funder was not involved in the study design, collection, analysis, interpretation of data, the writing of this article or the decision to submit it for publication.

Abbreviations

The following abbreviations are used throughout the manuscript:

CE	Counter electrode
CPP	Cyclic potentiodynamic polarization
E_{corr}	Corrosion potential
EV	Electric vehicle
ICE	Internal combustion engine
i_{corr}	Corrosion current density
OM	Optical microscope
RE	Reference electrode
R_p	Polarization resistance
WBL	Water-based lubricant
WE	Working electrode
WMEG	50% dilution of DI water and ethylene glycol
WGlycerol	50% dilution of DI water and glycerol
WPEG	50% dilution of DI water and polyethylene glycol
WPAG	50% dilution of DI water and polyalkylene glycol
β	Tafel slope
α_0	Pressure–viscosity coefficient

References

1. Ahmed Abdalglil Mustafa, W.; Dassenoy, F.; Sarno, M.; Senatore, A. A review on potentials and challenges of nanolubricants as promising lubricants for electric vehicles. *Lubr. Sci.* **2022**, *34*, 1–29. [CrossRef]
2. Sosa, Y. Design requirements and challenges for single electric vehicle fluids. *Tribol. Lubr. Technol.* 2023. Available online: https://www.stle.org/files/TLTArchives/2023/08_August/Feature.aspx (accessed on 20 August 2023).
3. Cornwell, K. *Electric Drivelines Challenge Traditional Tests*; Lubes and Greases: Falls Church, VA, USA, 2018; Available online: https://www.lubesngreases.com/magazine/24_10/electric-drivelines-challenge-traditional-tests/ (accessed on 30 August 2022).
4. Farfan-Cabrera, L.I. Tribology of electric vehicles: A review of critical components, current state and future improvement trends. *Tribol. Int.* **2019**, *138*, 473–486. [CrossRef]
5. Rahman, M.H.; Warneke, H.; Webbert, H.; Rodriguez, J.; Austin, E.; Tokunaga, K.; Rajak, D.K.; Menezes, P.L. Water-Based Lubricants: Development, Properties, and Performances. *Lubricants* **2021**, *9*, 73. [CrossRef]
6. Matta, C. Influence of New Emerging E-Fluids Technologies on Rolling/Sliding Contacts. In Proceedings of the STLE 2022, Orlando, FL, USA, 15–19 May 2022.
7. Zhang, C.H.; Zhao, Y.C.; Björling, M.; Wang, Y.; Bin Luo, J.; Prakash, B. EHL Properties of Polyalkylene Glycols and Their Aqueous Solutions. *Tribol. Lett.* **2012**, *45*, 379–385. [CrossRef]
8. Shi, Y.; Minami, I.; Grahn, M.; Björling, M.; Larsson, R. Boundary and elastohydrodynamic lubrication studies of glycerol aqueous solutions as green lubricants. *Tribol. Int.* **2014**, *69*, 39–45. [CrossRef]
9. Yilmaz, M.; Mirza, M.; Lohner, T.; Stahl, K. Superlubricity in EHL Contacts with Water-Containing Gear Fluids. *Lubricants* **2019**, *7*, 46. [CrossRef]
10. Ge, X.; Halmans, T.; Li, J.; Luo, J. Molecular behaviors in thin film lubrication—Part three: Superlubricity attained by polar and nonpolar molecules. *Friction* **2019**, *7*, 625–636. [CrossRef]

11. Han, T.; Zhang, S.; Zhang, C. Unlocking the secrets behind liquid superlubricity: A state-of-the-art review on phenomena and mechanisms. *Friction* **2022**, *10*, 1137–1165. [CrossRef]
12. Sagraloff, N.; Dobler, A.; Tobie, T.; Stahl, K.; Ostrowski, J. Development of an Oil Free Water-Based Lubricant for Gear Applications. *Lubricants* **2019**, *7*, 33. [CrossRef]
13. Hirano, M.; Shinjo, K. Atomistic locking and friction. *Phys. Rev. B* **1990**, *41*, 11837–11851. [CrossRef] [PubMed]
14. Burbank, J.; Rausch, J.; Luther, R.; Kraft, G. New approaches to extreme friction reductions with lubricants. In Proceedings of the 22nd International Colloquium Tribology, Ostfildern, Germany, 28–30 January 2020.
15. Matta, C.; Joly-Pottuz, L.; De Barros Bouchet, M.I.; Martin, J.M.; Kano, M.; Zhang, Q.; Goddard, W.A. Superlubricity and tribochemistry of polyhydric alcohols. *Phys. Rev. B* **2008**, *78*, 085436. [CrossRef]
16. Habchi, W.; Matta, C.; Joly-Pottuz, L.; De Barros, M.I.; Martin, J.M.; Vergne, P. Full Film, Boundary Lubrication and Tribochemistry in Steel Circular Contacts Lubricated with Glycerol. *Tribol. Lett.* **2011**, *42*, 351–358. [CrossRef]
17. Joly-Pottuz, L.; Martin, J.M.; De Barros Bouchet, M.I.; Belin, M. Anomalous Low Friction Under Boundary Lubrication of Steel Surfaces by Polyols. *Tribol. Lett.* **2008**, *34*, 21–29. [CrossRef]
18. Chen, Z.; Liu, Y.; Zhang, S.; Luo, J. Controllable Superlubricity of Glycerol Solution via Environment Humidity. *Langmuir* **2013**, *29*, 11924–11930. [CrossRef] [PubMed]
19. Li, J.; Zhang, C.; Ma, L.; Liu, Y.; Luo, J. Superlubricity Achieved with Mixtures of Acids and Glycerol. *Langmuir* **2013**, *29*, 271–275. [CrossRef] [PubMed]
20. Tamayo, J.G.Z.; Björling, M.; Shi, Y.; Prakash, B.; Larsson, R. Micropitting performance of glycerol-based lubricants under rolling-sliding contact conditions. *Tribol. Int.* **2022**, *167*, 107348. [CrossRef]
21. Hofmann, S.; Lohner, T.; Stahl, K. Influence of water content on elastohydrodynamic friction and film thickness of water-containing polyalkylene glycols. *Front. Mech. Eng.* **2023**, *9*, 1128447. [CrossRef]
22. Hofmann, S.; Hou, J.; Lohner, T.; Stahl, K. Elastohydrodynamic Lubrication Mechanisms of Aqueous Polyethylene Glycols. *Tribol. Lett.* **2025**, *73*, 41. [CrossRef]
23. Wijanarko, W.; Khanmohammadi, H.; Espallargas, N. Ionic Liquid Additives in Water-Based Lubricants for Bearing Steel—Effect of Electrical Conductivity and pH on Surface Chemistry, Friction and Wear. *Front. Mech. Eng.* **2022**, *7*, 756929. [CrossRef]
24. Wen, X.; Peng, G.; Bai, P.; Yuan, N.; Yue, L.; Meng, Y.; Tian, Y.; Li, L.; Ding, J. Tribocorrosion behavior of GCr15 steel in water–glycol fire-resistant hydraulic fluids (HFC) containing seawater. *J. Mater. Res. Technol.* **2024**, *30*, 4682–4691.
25. Roberge, P.R. *Handbook of Corrosion Engineering*; McGraw-Hill: New York, NY, USA, 1999.
26. Zhang, X.; Liu, X.; Dong, W.; Fan, E.; Bai, Z.; Hu, G.; Yi, P.; Xiao, K.; Huang, Y. Corrosion behavior of AISI321 stainless steel in an ethylene glycol-water solution. *Int. J. Electrochem. Sci.* **2019**, *14*, 2683–2692. [CrossRef]
27. Palcut, M.; Gerhátová, Ž.; Šulhánek, P.; Gogola, P. Corrosion Resistance of Steel S355MC in Crude Glycerol. *Technologies* **2023**, *11*, 69. [CrossRef]
28. Wang, J.; Wang, L.; Li, H.; Qu, N. Pitting corrosion inhibition of honeycomb seal using glycerol-water electrolyte in electrochemical grinding. *Electrochim. Acta* **2025**, *539*, 147092. [CrossRef]
29. Zubaidi, I.A.; Jones, R.; Alzughaibi, M.; Albayyadhi, M.; Darzi, F.; Ibrahim, H. Crude Glycerol as an Innovative Corrosion Inhibitor. *Appl. Syst. Innov.* **2018**, *1*, 12. [CrossRef]
30. Boudellioua, H.; Hamlaoui, Y.; Tifouti, L.; Pedraza, F. Effects of polyethylene glycol (PEG) on the corrosion inhibition of mild steel by cerium nitrate in chloride solution. *Appl. Surf. Sci.* **2019**, *473*, 449–460. [CrossRef]
31. Santambrogio, M.; Perrucci, G.; Trueba, M.; Trasatti, S.P.; Casaletto, M.P. Effect of major degradation products of ethylene glycol aqueous solutions on steel corrosion. *Electrochim. Acta* **2016**, *203*, 439–450. [CrossRef]
32. Esenin, V.N.; Denisovich, L.I. Contact corrosion of metals in aqueous and aqueous organic environments: III. Corrosion of metals aqueous glycol solutions with high water contents. *Prot. Met. Phys. Chem. Surf.* **2009**, *45*, 595–599. [CrossRef]
33. Boonen, L.; Choukroun, D.; Azcona, I.N.; Nappini, S.; Magnano, E.; Cornelus, J.; Breugelmans, T. Corrosion inhibition of copper in glycol-based heat transfer fluids: A comparative gravimetric and electrochemical study. *Corros. Sci.* **2026**, *265*, 113822. [CrossRef]
34. Bosch, J.; DellaCorte, C. Rheological Characterization and Tribological Evaluation of Water-Based Lubricants in AISI 52100 Bearing Steel. *Tribol. Lett.* **2024**, *72*, 10. [CrossRef]
35. Bair, S.; Qureshi, F. Accurate Measurements of Pressure-Viscosity Behavior in Lubricants. *Tribol. Trans.* **2008**, *45*, 390–396. [CrossRef]
36. Samosir, R.; Budiarto; Simanjuntak, S.L.M.H. The influence of inhibitor Na_2CrO_4 and $NaNO_3$ on corrosion and micro structure on AISI 348 steel material. *IOP Conf. Ser. Mater. Sci. Eng.* **2017**, *237*, 012045. [CrossRef]
37. *ASTM G3-14*; Standard Practice for Conventions Applicable to Electrochemical Measurements in Corrosion Testing. ASTM International: West Conshohocken, PA, USA, 2019.
38. *ASTM G59-97*; Standard Test Method for Conducting Potentiodynamic Polarization Resistance Measurements. ASTM International: West Conshohocken, PA, USA, 2020.
39. Stern, M.; Geary, A.L. Electrochemical polarization. *J. Electrochem. Soc.* **1957**, *104*, 56. [CrossRef]

40. Jones, D.A. *Principles and Prevention of Corrosion*, 2nd ed.; Prentice Hall: Upper Saddle River, NJ, USA, 1996.
41. Bard, A.J.; Faulkner, L.R. *Electrochemical Methods: Fundamentals and Applications*; Wiley: Hoboken, NJ, USA, 2001.
42. *Standard's ASTM E986-04*; Standard Practice for Scanning Electron Microscope Beam Size Characterization. ASTM International: West Conshohocken, PA, USA, 2017.
43. Umoren, S.A.; Solomon, M.M. Recent developments on the use of polymers as corrosion inhibitors—A review. *Open Mater. Sci. J.* **2014**, *8*, 39–54. [CrossRef]
44. Verma, C.; Ebenso, E.E.; Quraishi, M.A.; Hussain, C.M. Recent developments in sustainable corrosion inhibitors: Design, performance and industrial scale applications. *Mater. Adv.* **2021**, *2*, 3806–3850. [CrossRef]
45. Khomami, M.N.; Danaee, I.; Attar, A.A.; Peykari, M. Effects of NO_2^- and NO_3^- ions on corrosion of AISI 4130 steel in ethylene glycol + water electrolyte. *Trans. Indian Inst. Met.* **2012**, *65*, 303–311. [CrossRef]
46. Guilminot, E.; Dalard, F.; Degrigny, C. Mechanism of iron corrosion in water–polyethylene glycol (PEG 400) mixtures. *Corros. Sci.* **2002**, *44*, 2199–2208. [CrossRef]
47. Zeman, G.J. *Corrosion Behavior of Several Metals in Ethylene Glycol-Base Heat-Transfer Fluids Under Conditions Encountered in Solar Energy Systems*; Argonne National Laboratory: Argonne, IL, USA, 1980. [CrossRef]
48. Dong, S.; La Plante, E.C.; Chen, X.; Torabzadegan, M.; Balonis, M.; Bauchy, M.; Sant, G. Steel corrosion inhibition by calcium nitrate in halide-enriched completion fluid environments. *npj Mater. Degrad.* **2018**, *2*, 32. [CrossRef]
49. Suraneni, P.; Azad, V.J.; Isgor, B.O.; Weiss, W.J. Calcium oxychloride formation in pastes containing supplementary cementitious materials: Thoughts on the role of cement and supplementary cementitious materials reactivity. *RILEM Tech. Lett.* **2016**, *1*, 24–30. [CrossRef]
50. Bastidas, D.M. Interpretation of impedance data for porous electrodes and diffusion processes. *Corrosion* **2007**, *63*, 515–521. [CrossRef]
51. Martin, U.; Ress, J.; Bosch, J.; Bastidas, D.M.M. Stress corrosion cracking mechanism of AISI 316LN stainless steel rebars in chloride contaminated concrete pore solution using the slow strain rate technique. *Electrochim. Acta* **2020**, *335*, 135565. [CrossRef]
52. Ribeiro, D.V.; Abrantes, J.C.C. Application of electrochemical impedance spectroscopy (EIS) to monitor the corrosion of reinforced concrete: A new approach. *Constr. Build. Mater.* **2016**, *111*, 98–104. [CrossRef]
53. Huang, J. Diffusion impedance of electroactive materials, electrolytic solutions and porous electrodes: Warburg impedance and beyond. *Electrochim. Acta* **2018**, *281*, 170–188. [CrossRef]
54. Brug, G.J.; van den Eeden, A.L.G.; Sluyters-Rehbach, M.; Sluyters, J.H. The analysis of electrode impedances complicated by the presence of a constant phase element. *J. Electroanal. Chem. Interfacial Electrochem.* **1984**, *176*, 275–295. [CrossRef]
55. Fajardo, S.; Llorente, I.; Jiménez, J.A.; Bastidas, J.M.; Bastidas, D.M. Effect of Mn additions on the corrosion behaviour of TWIP Fe-Mn-Al-Si austenitic steel in chloride solution. *Corros. Sci.* **2019**, *154*, 246–253. [CrossRef]
56. Huang, V.M.-W.; Vivier, V.; Orazem, M.E.; Pébère, N.; Tribollet, B. The apparent constant-phase-element behavior of a disk electrode with faradaic reactions. *J. Electrochem. Soc.* **2007**, *154*, C99. [CrossRef]
57. Hirschorn, B.; Orazem, M.E.; Tribollet, B.; Vivier, V.; Frateur, I.; Musiani, M. Determination of effective capacitance and film thickness from constant-phase-element parameters. *Electrochim. Acta* **2010**, *55*, 6218–6227. [CrossRef]
58. Martin, U.; Bosch, J.; Ress, J.; Bastidas, D.M. Long-term stability and electronic properties of passive film of lean-duplex stainless steel reinforcements in chloride containing mortar. *Constr. Build. Mater.* **2021**, *291*, 123319. [CrossRef]
59. Cornell, R.M.; Schwertmann, U. *The Iron Oxides: Structure, Properties, Reactions, Occurrences and Uses*, 2nd ed.; Completely Revised and Extended Edition; John Wiley & Sons: Hoboken, NJ, USA, 2006.
60. Revie, R.W.; Uhlig, H.H. *Corrosion and Corrosion Control: An Introduction to Corrosion Science and Engineering*; John Wiley & Sons: Hoboken, NJ, USA, 2008; 490p.
61. Khomami, M.N.; Danaee, I.; Attar, A.A.; Peykari, M. Kinetic and thermodynamic studies of AISI 4130 steel alloy corrosion in ethylene glycol-water mixture in presence of inhibitors. *Met. Mater. Int.* **2013**, *19*, 453–464. [CrossRef]
62. Samiento-Bustos, E.; Rodriguez, J.G.G.; Uruchurtu, J.; Dominguez-Patiño, G.; Salinas-Bravo, V.M. Effect of inorganic inhibitors on the corrosion behavior of 1018 carbon steel in the LiBr + ethylene glycol + H_2O mixture. *Corros. Sci.* **2008**, *50*, 2296–2303. [CrossRef]

Disclaimer/Publisher's Note: The statements, opinions and data contained in all publications are solely those of the individual author(s) and contributor(s) and not of MDPI and/or the editor(s). MDPI and/or the editor(s) disclaim responsibility for any injury to people or property resulting from any ideas, methods, instructions or products referred to in the content.